

Integer Quantum Magnon Hall Plateau-Plateau Transition in a Spin Ice Model

Baolong Xu,^{1,2} Tomi Ohtsuki,³ and Ryuichi Shindou^{1,2,*}

¹International Center for Quantum Materials, Peking University, Beijing 100871, China

²Collaborative Innovation Center of Quantum Matter, Beijing 100871, China

³Department of Physics, Sophia University, Chiyoda-ku, Tokyo 102-8554, Japan

(Dated: December 15, 2016)

Low-energy magnon bands in a two-dimensional spin ice model become integer quantum magnon Hall bands under an out-of-plane field. By calculating the localization length and the two-terminal conductance of magnon transport, we show that the magnon bands with disorders undergo a quantum phase transition from an integer quantum magnon Hall regime to a conventional magnon localized regime. Finite size scaling analysis as well as a critical conductance distribution shows that the quantum critical point belongs to the same universality class as that in the quantum Hall transition. We characterize thermal magnon Hall conductivity in disordered quantum magnon Hall system in terms of robust chiral edge magnon transport.

PACS numbers:

Bosonic analogue of integer quantum Hall states have been proposed in a number of quasi-particle boson systems with broken time-reversal symmetry such as photon,¹⁻⁶ phonon,⁷ exciton,⁸ exciton-polariton,⁹ triplon,¹⁰ magnon¹¹⁻¹⁹ and surface magnon-polariton.²⁰ Typically, their quasi-particle excitations have extended bulk bands with topological integers and topological edge modes whose chiral dispersions cross band gaps among these bulk bands. Due to its chiral (unidirectional) nature, a quasi-particle boson flow along the edge mode is believed to be robust against generic elastic backward scatterers, fostering a rich prospect of their future applications.^{1-9,11-13,20} On the one hand, these bosonic systems often *break conservation of the quasi-particle number* even at the level of respective quadratic Hamiltonian.^{8,9,11-16,19,21-27} Thereby, one naturally wonders if the quasi-particle flow along the topological edge modes is still robust against such particle-number-non-conserving perturbations or not. In other words, one may raise a question whether two quantum Hall regimes with different Chern integers are topologically distinguishable even in the absence of the U(1) symmetry associated with the quasi-particle number conservation.

In this rapid communication, we study effects of generic disorder potentials in a simplest spin model in a quantum magnon Hall regime. Our numerical results and the following argument clarify that, even without the explicit U(1) symmetry at the Hamiltonian level, the topological magnon edge mode provides a robust quantized magnon conductance and therefore quantum magnon Hall regimes with different topological integers are always distinguished by a quantum critical point with delocalized bulk magnon band. Thermal conductance distributions calculated at the critical point clearly shows that the quantum critical point belongs to the same universality class as the two-dimensional integer quantum Hall plateau-plateau transition. Based on these knowledge, we give a generic expression for the thermal Hall conductivity in disordered integer quantum bosonic Hall systems from edge transport picture.

We study spin excitations in a square-lattice spin ice model²⁸⁻³¹ under out-of-plane Zeeman field H_Z ;

$$H = \sum_{\langle i,j \rangle} \frac{1}{|\mathbf{i} - \mathbf{j}|^3} (\hat{S}_i \cdot \hat{S}_j - 3(\hat{S}_i \cdot \mathbf{n}_{ij})(\hat{S}_j \cdot \mathbf{n}_{ij})) - D \sum_{i \in A} (\hat{S}_i^x)^2 - D \sum_{j \in B} (\hat{S}_j^y)^2 - H_Z \sum_{i \in A, B} \hat{S}_i^z. \quad (1)$$

The model consists of two inequivalent spins in a unit cell, A -sublattice spin $S_{i \in A}$ on the x -link of the square lattice and B -sublattice spins $S_{i \in B}$ on the y -link.³² Due to a magnetic shape anisotropy,²⁸⁻³² each sublattice spin has an easy-axis anisotropy D (> 0) along respective spatial direction. Heisenberg spins are coupled with each other by magnetic dipole-dipole interaction, \mathbf{n}_{ij} denotes the unit vector connecting sites \mathbf{i} and \mathbf{j} . An inclusion of the next and the next nearest neighbor magnetic dipolar couplings imposes so-called two-in two-out ice rule for each vertex, which has been experimentally observed in a patterned ferromagnetic film.²⁸

When the classical ground-state spin configuration becomes fully polarized by the Zeeman field ($H_Z > H_s \simeq DS$), the lowest magnon band and the second lowest magnon band acquire the topological number with opposite sign due to the finite next nearest neighbor dipolar coupling, and a topological chiral edge mode appears inside a band gap between the two.³² The corresponding magnon Hamiltonian is obtained from Eq. (1) with $S_{z,j} \equiv S - b_j^\dagger b_j$, $S_{-,j} \equiv b_j^\dagger \sqrt{2S}$, $S_{+,j} \equiv b_j \sqrt{2S}$ as,

$$\begin{aligned} H_b &\equiv H_{\text{on}} + H_{\text{nn}} + H_{\text{nnn}} \\ H_{\text{on}} &\equiv \frac{1}{2} \sum_{j \in A} \{ (D + d_j) S (-b_j^{\dagger 2} - b_j^\dagger b_j) + (H_Z + h_j) b_j^\dagger b_j \} \\ &+ \frac{1}{2} \sum_{j \in B} \{ (D + d_j) S (b_j^{\dagger 2} - b_j^\dagger b_j) + (H_Z + h_j) b_j^\dagger b_j \} + \text{h.c.} \end{aligned}$$

$$\begin{aligned}
\mathbf{H}_{\text{nn}} &\equiv \sum_{m=1,2} \sum_{\mathbf{j} \in A} \sum_{\mathbf{i}=\mathbf{j} \pm \delta_m, \mathbf{i} \in B} \\
\frac{JS}{4} &(b_{\mathbf{j}}^\dagger b_{\mathbf{i}} - 2b_{\mathbf{i}}^\dagger b_{\mathbf{i}} - 2b_{\mathbf{j}}^\dagger b_{\mathbf{j}} + 6i(-1)^m b_{\mathbf{j}}^\dagger b_{\mathbf{i}}^\dagger + \text{h.c.}) \\
\mathbf{H}_{\text{nnn}} &\equiv \sum_{\alpha=A,B} \sum_{m=1,2} \sum_{\mathbf{j} \in \alpha} \sum_{\mathbf{i}=\mathbf{j} \pm e_m} \\
\frac{J'_{\alpha,m} S}{4} &(-b_{\mathbf{j}}^\dagger b_{\mathbf{i}} - b_{\mathbf{i}}^\dagger b_{\mathbf{i}} - b_{\mathbf{j}}^\dagger b_{\mathbf{j}} + 3(-1)^m b_{\mathbf{j}}^\dagger b_{\mathbf{i}}^\dagger + \text{h.c.}) \quad (2)
\end{aligned}$$

where J , $J'_{\alpha,m}$ denote the nearest and the next nearest dipolar interaction, respectively with $J'_{A,1} = J'_{B,2} = J'_1$ and $J'_{A,2} = J'_{B,1} = J'_2$. e_1 and e_2 are the primitive lattice vectors of the square lattice and $2\delta_m = e_1 - (-1)^m e_2$ ($m = 1, 2$).³² Short-ranged randomness are introduced in Eq. (2); $d_{\mathbf{j}}$ and $h_{\mathbf{j}}$ are uniformly distributed within $[-W_D, W_D]$ and $[-W_H, W_H]$. We set the unit of energy to be JS and that of length the lattice spacing. Due to magnetic anisotropy term, dipolar interaction and randomness, the quadratic boson Hamiltonian does not have any continuous $U(1)$ symmetry associated with magnon

number conservation.

Using the transfer matrix method,^{34–36} we first calculated the localization length of a single-particle eigenstate of a corresponding generalized eigenvalue problem with the randomness. Due to the bosonic nature, the eigenvalue problem takes a form of $\mathcal{H}_{\text{BdG}}|\phi\rangle \equiv \sigma_3|\phi\rangle E$, with $\Psi \equiv [\cdots, b_{\mathbf{j},A}, b_{\mathbf{j},B}, \cdots, b_{\mathbf{j},A}^\dagger, b_{\mathbf{j},B}^\dagger, \cdots]^T$ and $\mathbf{H}_b \equiv \Psi^\dagger \mathcal{H}_{\text{BdG}} \Psi$. σ_3 in the right hand side is a 2 by 2 diagonal Pauli matrix in the particle-hole space; $\sigma_3 \Psi \equiv [\cdots, +b_{\mathbf{j},A}, +b_{\mathbf{j},B}, \cdots, -b_{\mathbf{j},A}^\dagger, -b_{\mathbf{j},B}^\dagger, \cdots]^T$ and E is an eigenenergy to which $|\phi\rangle$ belongs. We consider a quasi-one-dimensional (q1d) geometry, where the system is spatially larger in one direction (x -direction) than in the other (y -direction). For every j_x ($j_x = 1, \cdots, L$) with $\mathbf{j} \equiv (j_x, j_y)$, the system has a finite width along the y -direction; $j_y = 1, \cdots, M$ with $M \ll L$. With $|\phi\rangle \equiv [|B_{j_x=1}\rangle, \cdots, |B_{j_x}\rangle, \cdots, |B_{j_x=L}\rangle]^T$ and $|B_{j_x}\rangle \equiv [\phi_{j_x, j_y=1, A}, \cdots, \phi_{j_x, j_y=M, B}^*]^T$, the generalized eigenvalue equation takes a following $8M \times 8M$ matrix form;

$$\begin{pmatrix} |B_{j_x+1}\rangle \\ H_+ |B_{j_x}\rangle \end{pmatrix} = \begin{pmatrix} -H_-^{-1}(H_{j_x} - E\sigma_3) & -H_-^{-1} \\ H_+ & 0 \end{pmatrix} \begin{pmatrix} |B_{j_x}\rangle \\ H_+ |B_{j_x-1}\rangle \end{pmatrix} \equiv T_{j_x} \begin{pmatrix} |B_{j_x}\rangle \\ H_+ |B_{j_x-1}\rangle \end{pmatrix} \equiv M_{j_x} \begin{pmatrix} |B_1\rangle \\ H_+ |B_0\rangle \end{pmatrix}, \quad (3)$$

and $M_n \equiv \prod_{j_x=1}^n T_{j_x}$. Note that H_{j_x} differs from one another for different j_x due to the on-site randomness, while H_\pm are the same for different j_x with $H_+ \equiv H_-^\dagger$. An $8M$ by $8M$ matrix T_{j_x} has a symplectic feature; $T_{j_x}^{-1} = \tau_y T_{j_x}^\dagger \tau_y$, with τ_y being a Pauli matrix in the 2-dimensional space subtended by $|B_{j_x}\rangle$ and $H_+ |B_{j_x-1}\rangle$. Thus, $T_{j_x}^\dagger T_{j_x}$ has a pair of two positive eigenvalues; $\alpha_1, 1/\alpha_1, \alpha_2, 1/\alpha_2, \cdots$. The same holds true for $M_n^\dagger M_n$. Call a set of all eigenvalues of an Hermitian matrix $P_n \equiv M_n^\dagger M_n$ as $e^{2n/\lambda_1}, e^{-2n/\lambda_1}, e^{2n/\lambda_2}, e^{-2n/\lambda_2}, \cdots$ with $0 < 1/\lambda_1 < 1/\lambda_2 < \cdots$. For sufficiently large n , all real $1/\lambda_j$ converge into finite values (Lyapunov exponents; LE).³⁷ Using the Gram-Schmidt orthonormalization, we numerically obtained the smallest LE of P_n ($1/\lambda_1$) for larger n ; $n = 10^5 \sim 10^6$. λ_1 is nothing but the largest localization length of the eigenstate of the q1d system at energy E .³⁴ We set E inside the topological band gap in the clean limit.

With weaker randomness, the localization length λ_1 normalized by M decreases on increasing M , suggesting that eigenstates in this regime are all localized due to the topological band gap (quantum magnon Hall regime). The same observations hold true with much stronger randomness, indicating that eigenstates in much stronger disordered region belong to a conventional Anderson localized regime. Obtained numerical result (Fig. 1) shows that these two localized regions are always separated by a quantum phase transition point where the normalized

localization length barely changes as a function of M . The scale invariant behaviour of λ_1/M suggests the existence of a quantum phase transition similar to an integer quantum Hall plateau-plateau transition.^{36,38}

To confirm this, we further calculate the two-terminal magnon conductance G for the $M \times L$ system from a transmission matrix $\mathbf{t} \equiv \mathbf{T}_{11}^{-1}$ as $hG \equiv \text{Tr}[\mathbf{t}^\dagger \mathbf{t}]$. The transmission matrix is calculated from the transfer matrix; $[\mathbf{T}_{11}]_{lm} = \mathbf{y}_{l,+}^\dagger \tau_y (\prod_{j_x=1}^L T_{j_x}) \mathbf{y}_{m,+}$, with $\sqrt{|J_{m,+}} \mathbf{y}_{m,+} \equiv \mathbf{x}_{m,+}$ and $\mathbf{J}_{m,+} \equiv \mathbf{x}_{m,+}^\dagger \tau_y \mathbf{x}_{m,+}$. Here we choose $\mathbf{x}_{m,+}$ to be eigenstates of a model of decoupled one-dimensional chains; $\mathbf{H}_{\text{lead}} = \sum_{\nu=A,B} \sum_{\mathbf{j}} (tb_{(j_x+1, j_y), \nu}^\dagger b_{(j_x, j_y), \nu} + \text{h.c.} + \mu b_{\mathbf{j}, \nu}^\dagger b_{\mathbf{j}, \nu})$. The conductance along the x -direction is calculated both with open (G_o) and with periodic boundary conditions (G_p) along the y -direction.

G_o thus calculated tends to have a finite quantized plateau in the quantum magnon Hall regime in the thermodynamic limit ($G_o = \frac{1}{h}$), while showing zero conductance in the conventional localized regime (Fig. 2). The quantization in the quantum magnon Hall regime demonstrates a robust unidirectional magnon transport along the topological chiral edge mode. The bulk conductance seen by G_p tends to have a finite value only at the transition point, while zero otherwise in larger system size. These observations lead to the conclusion that the quantum magnon Hall regime with the robust chiral edge mode and the conventional Anderson localized

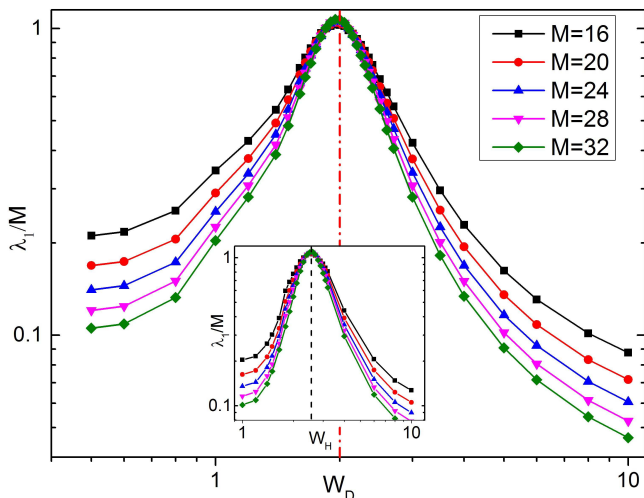


FIG. 1: (color online) Localization length calculated for different system size M as a function of disorder strength for the magnetic anisotropy W_D , with $H_Z = 15$, $DS = 2.2$, $JS = 1.0$, $J'_1S = 0.35$, $J'_2S = 0.28$. The eigenenergy E is set inside the band gap ($E = 3.3$). (Inset) Localization length as a function of disorder strength for the Zeeman field W_H , with the same set of other parameters. Black broken/red dash dotted lines denote scale-invariant points of λ_1/M in the presence of finite W_H/W_D respectively.

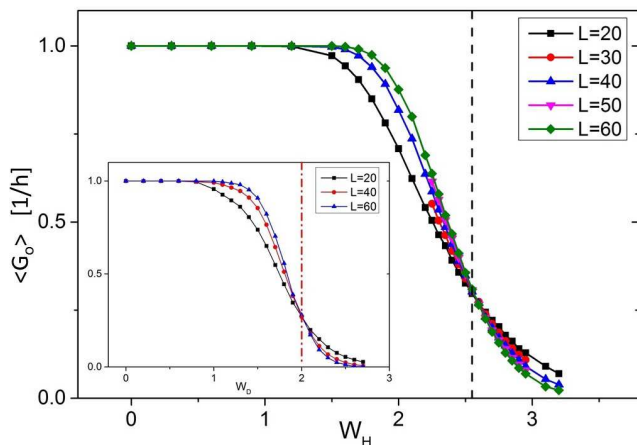


FIG. 2: (color online) Two-terminal conductance along the x -direction with open boundary condition in the y -direction G_o as a function of disorder strength for the field W_H (inset; as a function of disorder strength for the anisotropy W_D). The lattice geometry is chosen to be a rectangular with $2M = L$ ($L = 20 \sim 60$). Other parameters are set to be the same as in Fig. 1. Black broken/red dash dotted lines denote the scale-invariant points of λ_1/M shown in Fig. 1.

regime without the edge mode are topologically disconnected by a direct transition point with a delocalized bulk state. Importantly, this holds true irrespectively of the presence of the explicit $U(1)$ symmetry at the Hamiltonian level.

Robustness of chiral magnon edge transports against

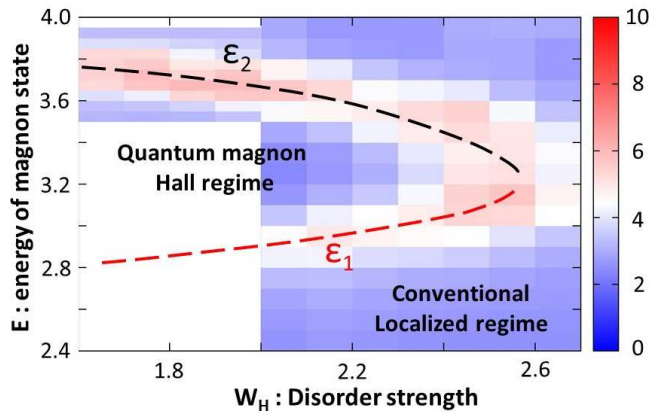


FIG. 3: (color online) Phase diagram subtended by the disorder strength W_H and single-magnon energy E . The phase boundaries between quantum magnon Hall regime with the quantized edge conductance ($G_o = \frac{1}{h}$) and conventional Anderson localized regime, such as $E = \mathcal{E}_1(W_H)$ and $E = \mathcal{E}_2(W_H)$, are determined from the size dependence of the two-terminal conductance with periodic boundary condition G_p .³² Color plot refers to $-\log \sigma$ where σ is a standard deviation of G_p with different system size L ; $\mathcal{N}\sigma^2 \equiv \sum_L (G_{p,L} - \overline{G_p})^2$ and $\mathcal{N}\overline{G_p} \equiv \sum_L G_{p,L}$ with \mathcal{N} the number of system sizes. Note that near the scale invariant points, σ^2 becomes small, hence larger $-\log \sigma^2$. The parameters are taken to be the same as in Fig. 1.

boson-number-non-conserving elastic perturbations is a consequence of the energy conservation. Our BdG type Hamiltonian has a particle-hole symmetry, $\sigma_1 \mathcal{H}_{\text{BdG}} \sigma_1 = \mathcal{H}_{\text{BdG}}^*$, where σ_1 exchanges particle and hole indices; $\sigma_1 \Psi \equiv [\dots, b_{j,A}^\dagger, b_{j,B}^\dagger, \dots, b_{j,A}, b_{j,B}, \dots]$. Due to this generic symmetry, any eigenstate $|\phi\rangle$ of \mathcal{H}_{BdG} has its particle-hole counterpart $|\bar{\phi}\rangle \equiv \sigma_1(|\phi\rangle)^*$. A local perturbation which does not conserve the boson number can have a finite matrix element between these two, e.g. $\langle \phi | \mathcal{H}' | \bar{\phi} \rangle \neq 0$ with $\mathcal{H}' = b_i^\dagger b_i^\dagger + \text{h.c.}$. Physically, however, the hole state and the particle state are different number states of the same quasi-particle excitation, i.e. $|\bar{\phi}\rangle \propto |n-1\rangle$ and $|\phi\rangle \propto |n+1\rangle$, and the scattering process between these two is accompanied by an energy emission (or absorption) of $2E$, where E is an energy quantum for the quasi-particle excitation; $\mathcal{H}_{\text{BdG}}|\phi\rangle = \sigma_3|\phi\rangle E$ and $\mathcal{H}_{\text{BdG}}|\bar{\phi}\rangle = \sigma_3|\bar{\phi}\rangle(-E)$. Thus, any magnon state with $E > 0$ cannot be scattered into its hole counterpart by *elastic* scattering. In other words, particle and hole channels are completely decoupled both in the transmission matrix \mathbf{t} and in a reflection matrix \mathbf{r} in the two-terminal conductance calculation above. This results in the robustness of the chiral magnon edge transport even in the presence of boson-number-non-conserving perturbations. The decoupled nature of particle and hole channels also allows to define a magnon current even in the absence of the explicit $U(1)$ symmetry in the magnon Hamiltonian; the magnon continuity equation without the source term can be derived from the equation of motion for the Green

function as far as elastic scattering is concerned.

The robust chiral edge conductance in the quantum magnon Hall regime indicates that the Hall regime with the quantized edge conductance ($G_o = \frac{1}{h}$) is always disconnected from the conventional localized regime by a direct transition with delocalized bulk states.⁴⁷ This is indeed the case with a phase diagram subtended by the disorder strength W_H and the single-magnon energy E (Fig. 3). For a fixed W , the Hall regime is encompassed by the two direction transition points at $E = \mathcal{E}_1(W)$ and $\mathcal{E}_2(W)$. For $\mathcal{E}_1(W) < E < \mathcal{E}_2(W)$, G_o is quantized and G_p vanishes in the thermodynamic limit. For the other region, both G_o and G_p tend to vanish in a larger system size.³²

A finite-size scaling analyses of G_o (of Fig. 2) near the transition point ($W = W_c$) is carried out based on $G_o(L^{1/\nu}(W - W_c), L^{-|y|}) \simeq G_c + \sum_{n=1}^3 c_n(W - W_c)^n L^{n/\nu} + bL^{-|y|}$, with ν the critical exponent, y a scaling dimension of a leading-order irrelevant scaling field at the critical point and c_n fitting parameters.³⁹ For $L = 20, 30, 40, 50, 60$, the 95% confidence interval of ν is $[2.28, 2.60]$ with goodness of fit $Q = 0.003$. By omitting the smallest size, the estimate is $[2.54, 2.86]$ with goodness of fit $Q = 0.93$. Though being consistent with the recent estimate of ν of the quantum Hall universality class ($\nu \approx 2.59$),^{40–45} the error bars are too large to conclude this affirmatively. To this end, we further calculated distributions of the conductances at the critical point (Fig. 4). The distributions have striking similarities to the critical conductance distributions of the two-dimensional Chalker-Coddington network model,⁴⁶ which strongly suggests that the direct transition belongs to the quantum Hall universality class.

Based on these knowledge, let us finally characterize an edge-mode contribution to thermal magnon Hall conductivity κ_{xy} in the disordered quantum magnon Hall regime. To this end, we impose an open/periodic boundary condition along the y/x -direction, introduce a temperature gradient along the y -direction, and calculate an energy current along the x -direction. The energy Hall current is given as a function of the disorder strength W . For a given W , the system has sub-extensive number of chiral edge modes within $\mathcal{E}_1(W) < E < \mathcal{E}_2(W)$, where $G_o = \frac{1}{h}$. Thus, the edge modes within $[E, E + dE]$ give a magnon Hall current density of $\frac{dE}{hM}$, with M the system size along the y -direction. The energy Hall current density due to these chiral edge modes around $y = M$ with higher temperature T_H and that around $y = 0$ with lower temperature T_L are therefore,

$$I_{H/L}^{x,E} = \pm \frac{1}{hM} \int_{\mathcal{E}_1(W)}^{\mathcal{E}_2(W)} g(E, T_{H/L}) E dE,$$

respectively with Bose function $g(E, T) \equiv 1/[e^{E/k_B T} - 1]$. A sum of these two is proportional to the temperature gradient $\Delta_y T \equiv T_H - T_L$; $I_t^{x,E} \equiv I_H^{x,E} + I_L^{x,E} = \kappa_{xy}^{\text{edge}} \partial_y T = \kappa_{xy}^{\text{edge}} \Delta_y T / M$. The thermal Hall conductivity

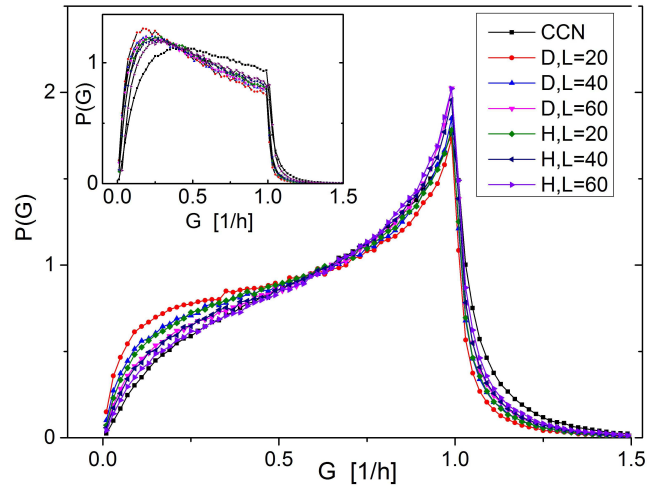


FIG. 4: (color online) Critical conductance distributions of G_o with $M = L$ with different system size ($L = 20, 40, 60$) and different types of randomness (either W_H or W_D). The black square points show the critical conductance distribution of the Chalker-Coddington network (CCN) model. The energy E and the other parameters are the same as in Figs. 1 and 2, respectively. The critical values of W_H and W_D are chosen to be a scale invariant point of G_o . (Inset) Critical conductance distribution of G_p and its comparison with that of the CCN model.

ity takes a form;

$$\kappa_{xy}^{\text{edge}}(W) = -\frac{k_B^2 T}{h} \left(C_2(g(\mathcal{E}_2, T)) - C_2(g(\mathcal{E}_1, T)) \right), \quad (4)$$

with $T \equiv \frac{T_H + T_L}{2}$ and $C_2(x)$ is a non-analytic function; $C_2(x) \equiv \int_0^x (\ln \frac{1+t}{t})^2 dt$. The above argument can be easily generalized into generic quantum magnon Hall systems with disorders.³² Note also that the edge-mode contribution dominates total κ_{xy} in a system with the quasi-one-dimensional geometry ($M \ll L$), where a bulk contribution diminishes as $e^{-aL/M}$ (a being a constant of the order of 1) due to the localization effect in one-dimensional systems.

In this rapid communication, we studied low-energy magnon bands in a two-dimensional spin ice model with disorders. We show that the magnon bands with disorders undergo a direct transition from an integer quantum magnon Hall regime to a conventional magnon localized regime. The critical conductance distributions at the transition point suggest that the direct transition belongs to quantum Hall universality class. The obtained result can be tested by standard microwave antennas experiments.³² Based on the edge magnon transport picture, we give a generic expression for thermal magnon Hall conductivity in *disordered* quantum magnon Hall systems. The obtained expression is qualitatively consistent with an expression of thermal magnon Hall conductivity in the clean limit, previously obtained based on the linear response theory.^{32,48–52}

The authors thank Junren Shi for fruitful discussions.

This work was supported by JSPS KAKENHI Grants No. 15H03700 and No. 24000013 and by NBRP of China

(Grant No. 2015CB921104).

-
- * Electronic address: rshindou@pku.edu.cn
- ¹ F. D. M. Haldane and S. Raghu, Phys. Rev. Lett. **100**, 013904 (2008).
 - ² S. Raghu and F. D. M. Haldane, Phys. Rev. A **78**, 033834 (2008).
 - ³ Z. Wang, Y. Chong, J. D. Joannopoulos, and M. Soljacic, Nature (London) **461**, 772 (2009).
 - ⁴ X. Ao, Z. Lin, and C. T. Chan, Phys. Rev. B, **80**, 033105 (2009).
 - ⁵ T. Ochiai and M. Onoda, Phys. Rev. B **80**, 155103 (2009).
 - ⁶ L. Lu, J. D. Joannopoulos, and M. Soljacic, Nat. Photonics. **8**, 821 (2014).
 - ⁷ E. Prodan, and C. Prodan, Phys. Rev. Lett. **103**, 248101 (2009).
 - ⁸ J. Yuen-Zhou, S. K. Saikin, N. Y. Yao, and A. Aspuru-Guzik, Nature Materials, **13**, 1026 (2014).
 - ⁹ T. Karzig, C.-E. Bardyn, N. Lindner, and G. Rafael, Phys. Rev. X, **5**, 031001 (2015).
 - ¹⁰ J. Romhányi, K. Penc, and R. Ganesh, Nature Comm. **6**, 6805 (2015).
 - ¹¹ R. Shindou, R. Matsumoto, S. Murakami and J. Ohe, Phys. Rev. B, **87**, 174427 (2013).
 - ¹² R. Shindou, J. Ohe, R. Matsumoto, S. Murakami, and E. Saitoh, Phys. Rev. B, **87**, 174402 (2013).
 - ¹³ R. Shindou and J. Ohe, Phys. Rev. B, **89**, 054420 (2014).
 - ¹⁴ L. Zhang, J. Ren, J. S. Wang, and B. Li, Phys. Rev. B, **87**, 144101 (2013).
 - ¹⁵ A. Mook, J. Henk, and I. Mertig, Phys. Rev. B, **91**, 174409 (2015).
 - ¹⁶ R. Chisnell, J. S. Helton, D. E. Freedman, D. K. Singh, R. I. Bewley, D. G. Nocera, and Y. S. Lee, Phys. Rev. Lett. **115**, 147201 (2015).
 - ¹⁷ A. Roldan-Molina, A. S. Nunez, and J. Fernandez-Rossier, New Journal of Physics, **18**, 045015 (2016).
 - ¹⁸ S. A. Owerre, Journal of Physics: Condensed Matter, **28**, 386001 (2016); Journal of Applied Physics, **120**, 043903 (2016).
 - ¹⁹ S. K. Kim, H. Ochoa, R. Zarzuela, and Y. Tserkovnyak, arXiv:1603.04827.
 - ²⁰ T. Ochiai, Science and Technology of Advanced Materials, **16**, 0.14401 (2015).
 - ²¹ G. Engelhardt, and T. Brandes, Phys. Rev. A, **91**, 053621, (2015).
 - ²² S. Furukawa, and M. Ueda, New. J. Phys. **17**, 115014 (2015).
 - ²³ B. Galilo, D. K. K. Lee, and R. Barnett, Phys. Rev. Lett. **115**, 245302 (2015).
 - ²⁴ G. Engelhardt, M. Benito, G. Platero, and T. Brandes, arXiv:1512.07653.
 - ²⁵ C. E. Bardyn, T. Karzig, G. Rafael, and T. C. H. Liew, Phys. Rev. B, **93**, 020502 (R) (2016).
 - ²⁶ V. Peano, M. Houde, C. Brendel, F. Marquardt, and A. A. Clerk, Nat. Comm. **7**, 10779 (2016).
 - ²⁷ Z. F. Xu, L. You, A. Hemmerich, and W. V. Liu, Phys. Rev. Lett. **117**, 085301 (2016).
 - ²⁸ R. F. Wang, C. Nisoli, R. S. Freitas, J. Li, W. McConville1, B. J. Cooley, M. S. Lund, N. Samarth, C. Leighton, V. H. Crespi and P. Schiffer, Nature **19**, 439 (2006).
 - ²⁹ Z. Budrikis, P. Politi, and R. L. Stamps, Phys. Rev. Lett. **105**, 017201 (2010).
 - ³⁰ Z. Budrikis, J. P. Morgan, J. Akerman, A. Stein, P. Politi, S. Langridge, C. H. Marrows, and R. L. Stamps, Phys. Rev. Lett. **109**, 037203 (2012).
 - ³¹ E. Iacocca, S. Gliga, R. L. Stamps, and O. Heinonen, Phys. Rev. B, **93**, 134420 (2016).
 - ³² See supplemental materials for detailed information of the square-lattice spin ice model, a phase diagram subtended by the disorder strength and energy of magnon state, microwave antennas experiment to test our theory results, a general expression of thermal Hall conductivity in disordered quantum magnon Hall systems and its qualitative consistency with the thermal magnon Hall conductivity in the clean limit previously obtained by the linear response theory.⁴⁸⁻⁵²
 - ³³ T. Holstein and H. Primakoff, Phys. Rev. **58**, 1098 (1940).
 - ³⁴ A. MacKinnon, and B. Kramer, Z. Phys. B, **53**, 1-13, (1983).
 - ³⁵ T.Ohtsuki, K. Slevin, and B. Kramer, Physica E (Amsterdam) **22**, 248 (2004).
 - ³⁶ B. Kramer, T. Ohtsuki, and S. Kettemann, Phys. Rep. **417**, 211 (2005).
 - ³⁷ V. I. Oseledec, Trans. Moscow Math. Soc. **19**, 197 (1968).
 - ³⁸ B. Huckestein, Rev. Mod. Phys. **67**, 357, (1995).
 - ³⁹ K. Slevin, and T. Ohtsuki, New J. Phys. **16**, 015012 (2014).
 - ⁴⁰ K. Slevin and T. Ohtsuki, Phys. Rev. B **80**, 041304 (2009).
 - ⁴¹ H. Obuse, A. R. Subramaniam, A. Furusaki, I.A. Gruzberg and A. W. W. Ludwig, Phys. Rev. B **82**, 035309 (2010).
 - ⁴² M. Amado, A. V. Malyshev, A. Sedrakyan and F. Dominguez-Adame, Phys. Rev. Lett. **107**, 066402 (2011).
 - ⁴³ I. C. Fulga, F. Hassler, A. R. Akhmerov and C. W. J. Beenakker, Phys. Rev. B **84** 245447 (2011).
 - ⁴⁴ J. P. Dahlhaus, J. M. Edge, J. Tworzydło and C. W. J. Beenakker, Phys. Rev. B **84**, 115133 (2011).
 - ⁴⁵ H. Obuse, I. A. Gruzberg and F. Evers, Phys. Rev. Lett. **109**, 206804 (2012).
 - ⁴⁶ J. T. Chalker and P. D. Coddington, J. Phys. C, **21**, 2665 (1988).
 - ⁴⁷ B. I. Halperin, Phys. Rev. B, **25**, 2185 (1982).
 - ⁴⁸ R. Matsumoto and S. Murakami, Phys. Rev. Lett. **106**, 197202 (2011).
 - ⁴⁹ R. Matsumoto and S. Murakami, Phys. Rev. B, **84**, 184406 (2011).
 - ⁵⁰ R. Matsumoto, R. Shindou, and S. Murakami, Phys. Rev. B, **89**, 054420 (2014).
 - ⁵¹ T. Qin, Q. Niu and J. R. Shi, Phys. Rev. Lett. **107**, 236601 (2011).
 - ⁵² T. Qin, J. Zhou, and J. R. Shi, Phys. Rev. B, **86**, 104305 (2012).

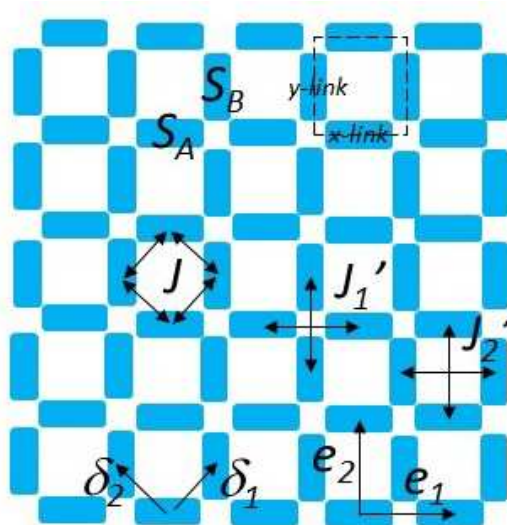


FIG. 5: (color online) Square-lattice spin ice model with two inequivalent ferromagnetic spins; $\mathbf{S}_{i \in A}$ and $\mathbf{S}_{i \in B}$ are on the center of the x -link and y -link of the square lattice respectively. The nearest neighbor dipole coupling strength is denoted by J , the next-nearest neighbor dipole coupling strengths are denoted by J'_1 and J'_2 ($J'_2 < J'_1$). e_1 and e_2 are the primitive lattice vectors of the square lattice. δ_1 and δ_2 connect the nearest neighbor spins; $\delta_1 \equiv \frac{e_1 + e_2}{2}$ and $\delta_2 \equiv \frac{e_1 - e_2}{2}$.

I. SUPPLEMENTAL MATERIALS FOR “INTEGER QUANTUM MAGNON HALL PLATEAU-PLATEAU TRANSITION IN A SPIN ICE MODEL”

II. TWO-DIMENSIONAL SPIN ICE MODEL UNDER STRONG OUT-OF-PLANE FIELD

A magnetic system considered consists of two inequivalent ferromagnetic ‘islands’ of the order of 100 nm size¹; one is centered on a x -link of a two-dimensional square lattice and the other is on a y -link (Fig. 5). The ferromagnetic island on the x/y -link is spatially elongated along the x/y -direction respectively. Thus, their magnetic moments prefer to point along the $\pm x/y$ -direction respectively due to the magnetic shape anisotropy. We model these two ferromagnetic islands as two inequivalent spins on the x/y -link with large magnetic moment S ($\mathbf{S}_{i \in A}/\mathbf{S}_{i \in B}$ respectively). The shape anisotropy is included as an effective single-ion spin-anisotropy energy such as $-D(S_{i \in A}^x)^2$ and $-D(S_{i \in B}^y)^2$. Ferromagnetic moments are coupled with one another via the magnetic dipole-dipole interaction¹, so do spins in the spin model. Based on the Holstein-Primakoff mapping, the corresponding quadratic magnon Hamiltonian is derived as in Eq. (2) (in the main text). For simplicity, we include only dipole couplings between the nearest neighbor spins (denoted by J : see Fig. 5) and between next nearest neighbor spins (denoted by $J'_{A,1} = J'_{B,2} = J'_1$ or $J'_{A,2} = J'_{B,1} = J'_2$: see Fig. 5). The ratio among these three are chosen to be consistent with the $1/r^3$ dipolar coupling strength (see below).

Without randomness ($\mathbf{d}_j \equiv \mathbf{h}_j \equiv 0$), the quadratic Hamiltonian given in Eq. (2) in the main text can be Fourier-transformed,

$$\mathbf{H}_b = \frac{1}{2} \sum_{\mathbf{k}} \begin{pmatrix} b_{\mathbf{k},A}^\dagger & b_{\mathbf{k},B}^\dagger & b_{-\mathbf{k},A} & b_{-\mathbf{k},B} \end{pmatrix} \cdot \mathbf{H}_{\text{BdG}}(\mathbf{k}) \cdot \begin{pmatrix} b_{\mathbf{k},A} \\ b_{\mathbf{k},B} \\ b_{-\mathbf{k},A}^\dagger \\ b_{-\mathbf{k},B}^\dagger \end{pmatrix},$$

$$\mathbf{H}_{\text{BdG}}(\mathbf{k}) = a_0(\mathbf{k})\gamma_0 + a_2(\mathbf{k})\gamma_2 + a_{14}(\mathbf{k})\gamma_{14} + a_{23}(\mathbf{k})\gamma_{23} + a_{45}(\mathbf{k})\gamma_{45}, \quad (5)$$

with

$$\gamma_j \equiv \sigma_j \otimes \tau_1, \quad \gamma_4 \equiv \sigma_0 \otimes \tau_2, \quad \gamma_5 \equiv \sigma_0 \otimes \tau_3, \quad \gamma_{\mu\nu} \equiv i\gamma_\mu \gamma_\nu, \quad (6)$$

where $j = 1, 2, 3$ and $\mu, \nu = 1, \dots, 5$. 2 by 2 Pauli matrix σ_j is for the particle-hole space, while 2 by 2 Pauli matrix

τ_j is for the A and B sublattices. Coefficients in Eq. (5) are

$$a_0(\mathbf{k}) = H_Z - DS - 4JS - J'S(\cos k_x + \cos k_y) - 4J'S, \quad (7)$$

$$a_2(\mathbf{k}) = -6JS \sin \frac{k_x}{2} \sin \frac{k_y}{2}, \quad a_{14}(\mathbf{k}) = DS, \quad (8)$$

$$a_{23}(\mathbf{k}) = 3J'S(\cos k_x - \cos k_y), \quad a_{45}(\mathbf{k}) = 2JS \cos \frac{k_x}{2} \cos \frac{k_y}{2}, \quad (9)$$

where we put $J'_1 = J'_2 \equiv J'$ for simplicity. The 4 by 4 matrix is diagonalized at every \mathbf{k} by a paraunitary transformation²

$$\mathbf{T}(\mathbf{k}) = e^{-i\theta_1\gamma_3} e^{i\frac{\pi}{4}\gamma_4} e^{\mu_1\gamma_1} e^{-i\theta_2\gamma_3} \begin{pmatrix} \cosh \mu_2 & 0 & -i \sinh \mu_2 & 0 \\ 0 & \cosh \mu_3 & 0 & -i \sinh \mu_3 \\ i \sinh \mu_2 & 0 & \cosh \mu_2 & 0 \\ 0 & i \sinh \mu_3 & 0 & \cosh \mu_3 \end{pmatrix}, \quad (10)$$

where $\theta_1, \theta_2, \mu_1, \mu_2$ and μ_3 are defined by a_0, a_2, a_{14}, a_{23} and a_{45} as follows;

$$\sin 2\theta_1 = \frac{a_{23}}{\sqrt{a_{23}^2 + a_2^2}}, \quad \cos 2\theta_1 = \frac{a_2}{\sqrt{a_{23}^2 + a_2^2}}, \quad (11)$$

$$\sin 2\theta_2 = \frac{\sqrt{a_{23}^2 + a_2^2} \frac{a_{14}}{\sqrt{a_0^2 - a_{14}^2}}}{\sqrt{a_{45}^2 + \left(\sqrt{a_{23}^2 + a_2^2} \frac{a_{14}}{\sqrt{a_0^2 - a_{14}^2}}\right)^2}}, \quad \cos 2\theta_2 = \frac{a_{45}}{\sqrt{a_{45}^2 + \left(\sqrt{a_{23}^2 + a_2^2} \frac{a_{14}}{\sqrt{a_0^2 - a_{14}^2}}\right)^2}}, \quad (12)$$

$$\sinh 2\mu_1 = \frac{a_{14}}{\sqrt{a_0^2 - a_{14}^2}}, \quad \cosh 2\mu_1 = \frac{a_0}{\sqrt{a_0^2 - a_{14}^2}}, \quad (13)$$

$$\sinh 2\mu_2 = \frac{b_{24}}{\sqrt{(b_0 + b_5)^2 - b_{24}^2}}, \quad \cosh 2\mu_2 = \frac{b_0 + b_5}{\sqrt{(b_0 + b_5)^2 - b_{24}^2}}, \quad (14)$$

$$\sinh 2\mu_3 = \frac{-b_{24}}{\sqrt{(b_0 - b_5)^2 - b_{24}^2}}, \quad \cosh 2\mu_3 = \frac{b_0 - b_5}{\sqrt{(b_0 - b_5)^2 - b_{24}^2}}, \quad (15)$$

with

$$b_0 \equiv \sqrt{a_0^2 - a_{14}^2}, \quad b_{24} \equiv \sqrt{a_{23}^2 + a_2^2} \frac{a_0}{\sqrt{a_0^2 - a_{14}^2}}, \quad b_5 \equiv \sqrt{a_{45}^2 + \left(\sqrt{a_{23}^2 + a_2^2} \frac{a_{14}}{\sqrt{a_0^2 - a_{14}^2}}\right)^2}. \quad (16)$$

In terms of the transformation, the BdG Hamiltonian is paraunitary equivalent to a diagonal matrix,

$$\mathbf{T}^\dagger(\mathbf{k}) \cdot \mathbf{H}_{\text{BdG}}(\mathbf{k}) \cdot \mathbf{T}(\mathbf{k}) = \begin{pmatrix} E_+(\mathbf{k}) & & & \\ & E_-(\mathbf{k}) & & \\ & & E_+(-\mathbf{k}) & \\ & & & E_-(-\mathbf{k}) \end{pmatrix}, \quad \mathbf{T}^\dagger(\mathbf{k}) \cdot \boldsymbol{\sigma}_3 \otimes \boldsymbol{\tau}_0 \cdot \mathbf{T}(\mathbf{k}) = \boldsymbol{\sigma}_3 \otimes \boldsymbol{\tau}_0,$$

where the two magnon energy bands are even functions in \mathbf{k} ;

$$E_\pm(\mathbf{k}) \equiv \sqrt{(b_0(\mathbf{k}) \pm b_5(\mathbf{k}))^2 - b_{24}^2(\mathbf{k})}. \quad (17)$$

Note that H_Z is sufficiently large that the lower magnon band $E_-(\mathbf{k})$ is fully gapped; $E_-(\mathbf{k}) > 0$ for $\forall \mathbf{k}$. This also allows that $a_0^2 - a_{14}^2 > 0$ and $b_0 > b_5$. In the absence of the next-nearest neighbor dipolar interaction $J' = 0$ ($a_{23} = 0$), two bands form a band touching with a massless Dirac dispersion at $\mathbf{k} = (0, \pi)$ and $(\pi, 0)$, where $a_{45} = a_2 = b_5 = 0$. The Dirac dispersions acquire a finite mass by non-zero next-nearest neighbor dipolar interaction and the sign of the mass is determined by that of J' . Due to this mass acquaintance, the upper magnon band ($E_+(\mathbf{k})$) and lower magnon band ($E_-(\mathbf{k})$) have ± 1 Chern integer respectively for $J' > 0$. When J' changes its sign from positive to negative, these two integers change into ∓ 1 respectively.

To calculate the Chern integer for the upper magnon band directly³⁻⁸, look into the first column of the paraunitary matrix $\mathbf{T}(\mathbf{k})$, which is nothing but a periodic part of the Bloch wavefunction for the upper magnon band,

$$\mathbf{T}(\mathbf{k}) = \begin{pmatrix} \frac{u_{1,+}(\mathbf{k})}{N_+} & \dots & \dots & \dots \\ \frac{u_{2,+}(\mathbf{k})}{N_+} & \dots & \dots & \dots \\ \frac{v_{1,+}(\mathbf{k})}{N_+} & \dots & \dots & \dots \\ \frac{v_{2,+}(\mathbf{k})}{N_+} & \dots & \dots & \dots \end{pmatrix}. \quad (18)$$

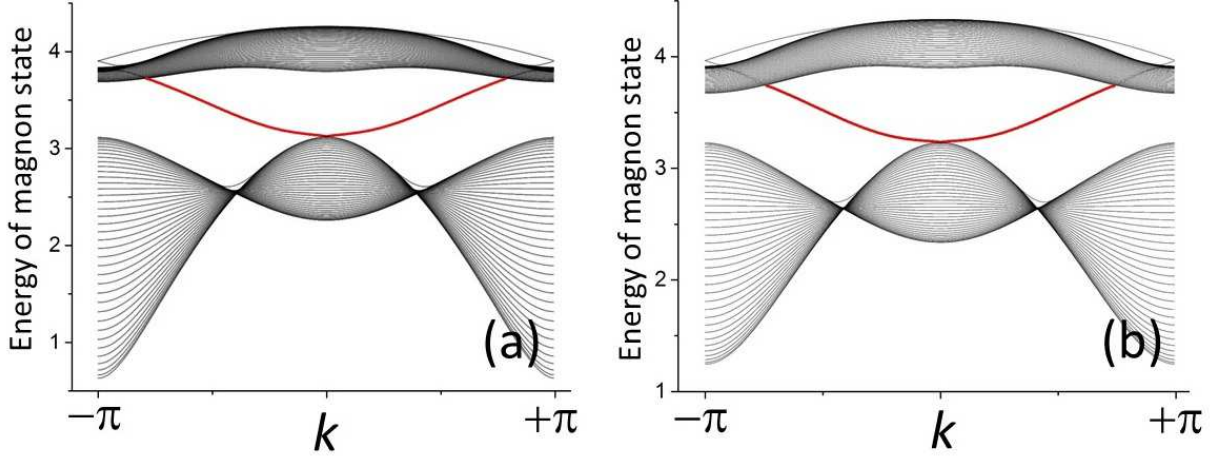


FIG. 6: (color online) Energy band dispersions of magnon states as function of the wave vector k , calculated with open/periodic boundary condition along the y/x -direction. Black colored dispersions are for bulk modes, and red colored dispersions are for the chiral edge modes; those at $k < 0$ are localized at $y = M (> 0)$ and those at $k > 0$ are localized at $y = 0$. (a) $J'_1 S = J'_2 S = 0.35$, $H_Z = 15.8$, $DS = 2.2$, $JS = 1.0$, (b) $J'_1 S = 0.35$, $J'_2 S = 0.28$, $H_Z = 15.8$, $DS = 2.2$, $JS = 1.0$.

where $u_{1,+}$ and $u_{2,+}$ ($v_{1,+}$ and $v_{2,+}$) are connected with each other by the C_4 rotation ($(k_x, k_y) \rightarrow (-k_y, k_x)$, exchanges A and B sublattices). $u_{j,+}$ and $v_{j,+}$ are connected with each other by a particle-hole transformation, which is generic in any quadratic boson Hamiltonian; $\boldsymbol{\sigma}_1 \cdot \mathbf{H}_{\text{BdG}}(\mathbf{k}) \cdot \boldsymbol{\sigma}_1 = \mathbf{H}_{\text{BdG}}^*(-\mathbf{k})$. $u_{1,+}(\mathbf{k})$ is given by

$$u_{1,+}(\mathbf{k}) = \cos(\theta_1 + \theta_2) \cosh \mu_1 \cosh \mu_2 + \sin(\theta_1 - \theta_2) \sinh \mu_1 \sinh \mu_2 \\ + i(\sin(\theta_1 - \theta_2) \cosh \mu_1 \cosh \mu_2 + \cos(\theta_1 + \theta_2) \sinh \mu_1 \sinh \mu_2). \quad (19)$$

while the other three are obtained from this by the C_4 rotation or by the particle-hole transformation. $\mathbf{T}(\mathbf{k})$ is given by a proper normalization; $N_+^2 \equiv u_{1,+}^2 + u_{2,+}^2 - v_{1,+}^2 - v_{2,+}^2$. By using Eqs. (7-16), one can see that $u_{1,+}$ (and also $v_{1,+}$) has a zero only at $\mathbf{k} = (0, \pi)$, while $u_{2,+}$ and $v_{2,+}$ have a zero at $\mathbf{k} = (\pi, 0)$. Thus, we expand $u_{1,+}(\mathbf{k})$ with respect to small \mathbf{q} with $\mathbf{k} \equiv (0, \pi) + \mathbf{q}$;

$$u_{1,+}((0, \pi) + \mathbf{q}) = \mathbf{X} \cdot \mathbf{q} + i\mathbf{Y} \cdot \mathbf{q} + \mathcal{O}(q^2), \quad (20)$$

where $\mathbf{X} \equiv (-a, -b)$, $\mathbf{Y} \equiv (a, -b)$. a and b are calculated as follows,

$$a = \frac{d\theta_1}{dk_x} \Big|_{\mathbf{k}=(0,\pi)} \left(\cosh \mu_1 \cosh \mu_2 - \sinh \mu_1 \sinh \mu_2 \right) = \frac{J}{4J'} \left(\cosh \mu_1 \cosh \mu_2 - \sinh \mu_1 \sinh \mu_2 \right) > 0 \\ b = \frac{d\theta_2}{dk_y} \Big|_{\mathbf{k}=(0,\pi)} \left(\cosh \mu_1 \cosh \mu_2 + \sinh \mu_1 \sinh \mu_2 \right) = \frac{JS\sqrt{a_0^2 - a_{14}^2}}{3\sqrt{2}J'SDS} \left(\cosh \mu_1 \cosh \mu_2 + \sinh \mu_1 \sinh \mu_2 \right) > 0.$$

for $J' > 0$ and $D > 0$. Note that $\mathbf{X} \times \mathbf{Y} = 2ab > 0$. Thus, a phase of $u_{1,+}(\mathbf{k})$, i.e. $\theta_{1,+}(\mathbf{k})$ with $u_{1,+} \equiv e^{i\theta_{1,+}}|u_{1,+}\rangle$, acquires $+2\pi$ phase holonomy, whenever \mathbf{k} rotates once around $(0, \pi)$ anti-clockwise. This dictates that the Chern integer for the upper band is $+1$ (that for the lower band is -1 due to the sum rule⁵). The non-zero topological integers for these two magnon bands result in a topological chiral magnon edge mode within the band gap⁵⁻¹⁰. The sign of the integer dictates that the mode has a chiral dispersion with the anti-clockwise rotation when viewed from $+z$ direction and the out-of-field is along $+z$ direction (“right-handed” chiral mode). So far, we assume that $J'_1 = J'_2 = J'$. For $J'_2 = 0.8J'_1$, we confirmed numerically that the same band gap with the chiral edge mode persists (Fig. 6).

III. A PHASE BOUNDARY BETWEEN THE QUANTUM MAGNON HALL REGIME AND CONVENTIONAL MAGNON LOCALIZED REGIME

A phase diagram in the main text (Fig. 3) has the quantum magnon Hall regime and conventional magnon localized regime. The boundary between these two regions is identified as a scale-invariant point of the two-terminal conductance calculated with the periodic boundary condition; G_p . Fig. 7 shows G_p as a function of the single-particle (magnon) energy E for several W . Thereby, we found two such scale-invariant points (one at $E = \mathcal{E}_1(W)$ specified by a black

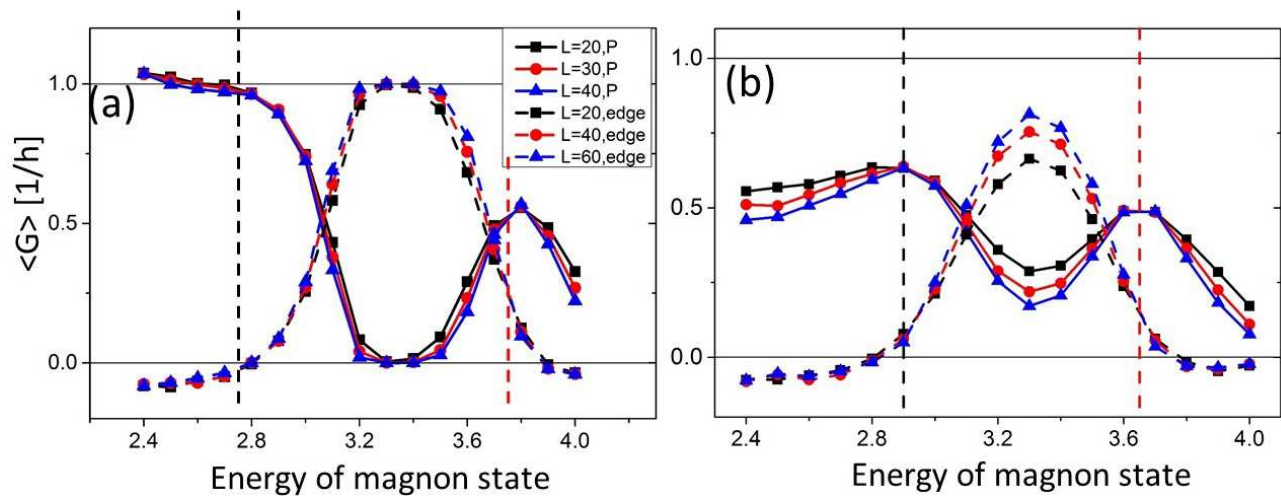


FIG. 7: (color online) Two-terminal conductance as a function of energy of magnon state E for several W ((a) $W = 1.3$ and (b) $W = 2.1$), calculated for the $L \times L$ system. Solid lines with different colors denote the conductance along the x -direction with periodic boundary condition along the y -direction G_p ; $L = 20$ (black), $L = 30$ (red), $L = 40$ (blue). Broken lines with different colors denote $G_o - G_p$, where G_o is the conductance with open boundary condition along the y -direction. The other parameters are the same as those given in the caption of Fig. 1 and 4 in the main text. Two direct transition points are identified as a scale-invariant point of G_p ; a red colored dotted line for $E = \mathcal{E}_2(W)$ and black colored dotted line for $E = \mathcal{E}_1(W)$. Note that, for $\mathcal{E}_1(W) < E < \mathcal{E}_2(W)$, $G_o - G_p$ has a tendency to take the quantized value ($1/h$) in the thermodynamic limit.

dotted line in Fig. 7 and the other at $E = \mathcal{E}_2(W)$ by a red dotted line). For $\mathcal{E}_1(W) < E < \mathcal{E}_2(W)$ an “edge conductance” characterized by $G_o - G_p$ has a tendency to take the quantized value ($1/h$) in the thermodynamic limit (G_o is the conductance along the x -direction with the open boundary condition along the y -direction). For $E < \mathcal{E}_1(W)$ or $E > \mathcal{E}_2(W)$, the edge conductance goes to zero. From these observations, we regard the former region as the quantum magnon Hall regime and the latter as the conventional magnon localized regime.

IV. MICROWAVE ANTENNAS EXPERIMENT

The two terminal magnon conductance calculated in the main text can be measured in a standard microwave experiment commonly used for spin wave experiments¹¹. The experiment consists of two microstrip microwave antennas attached to the two-dimensional square-lattice spin ice system (Fig. 8). The two antennas are spatially separated from each other shorter than a spin coherent length, over which spin wave propagates without an energy dissipation. Note that the spin coherent length in ferromagnetic insulator such as YIG can be over millimeters, while it is at most on the order of several micrometer in ferromagnetic metals.

The role of the first antenna is for spin wave excitation and that of the second antenna is for its detection. An a.c. electric current with a frequency in the microwave regime (let us call this as ‘external frequency’) is introduced in the first antenna (‘input signal’). The current locally excites spin wave with the same external frequency. The spin wave propagates through the magnonic crystal system, and, after a certain time, the spin wave reaches the second antenna, where an a.c. electric current is induced (‘output signal’).

The two terminal magnon conductance studied in the main text corresponds to a transmission ratio between the output electric current and input current. The ratio can be obtained as function of the external frequency within the microwave regime¹¹. When the frequency and the disorder strength are chosen inside the quantum magnon Hall regime, the transmission ratio is finite (see Fig. 3 of the main text; the frequency corresponds to energy of magnon states in the figure). Especially, the ratio is dominated by chiral edge spin wave transport, when the distance between two antennas is longer than the localization length. Namely, the bulk spin wave excited by the first antenna dies off quickly before it reaches the second antenna due to its finite localization length. Meanwhile, the chiral edge spin wave excited by the first antenna travels along the edge without being backward scattered.

When the frequency and the disorder are in the conventional magnon localized regime, the transmission ratio reduces dramatically. The ratio becomes exponentially small, if the localization length is much shorter than the distance between the two antennas. Accordingly, the quantum phase transition from the quantum magnon Hall regime to conventional magnon localized regime can be experimentally measurable through the dramatic reduction of

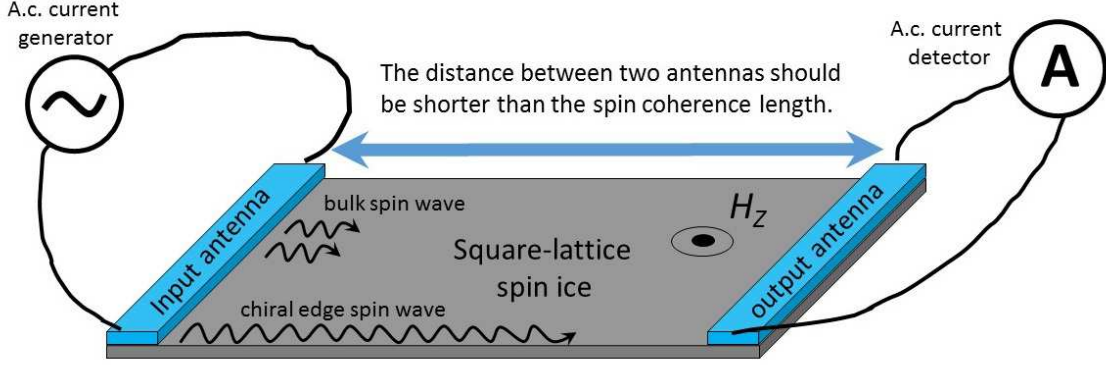


FIG. 8: A schematic picture for microwave antennas experiment. Two blue-colored bars denote the coplanar waveguide. The gray-colored plate denotes the two-dimensional patterned ferromagnetic film (square-lattice spin ice).

the transmission ratio as a function of either the external frequency or the disorder strength.

Note that the distance between the two antennas must be shorter than a finite spin coherence length (Fig. 8). The finite distance between the two antennas may result in a blurred change of the transmission ratio at the phase transition point. Nonetheless, the spin ice model made out of ferromagnetic insulator such as YIG allows a very large distance between the two antennas, e.g. 8mm in YIG¹¹. Since a typical localization length would be at largest on the order of micrometer scale¹², the very large spin coherence length in YIG may even enable us to study the critical properties of the quantum phase transition.

V. THERMAL MAGNON HALL CONDUCTIVITY IN GENERIC DISORDERED QUANTUM MAGNON HALL SYSTEMS AND ITS RELATION TO THE THERMAL MAGNON HALL CONDUCTIVITY IN THE CLEAN LIMIT

In the main text, we have studied only the model with two magnon bands. A realistic material may have more than two magnon bands, which have non-zero quantized Chern integers. Our study as well as established knowledge on interplays between localization effect and quantum Hall physics¹³ suggests that even small disorder makes all these bulk magnon bands localized except for delocalized bulk states at respective band center (Fig. 9(a,b)). A pair of two delocalized bulk states bound a mobility gap, inside which a topological chiral edge mode lives (Fig. 9(b)). For the two-band model studied in the main text, the bulk delocalized states at $E = \mathcal{E}_2$ and $E = \mathcal{E}_1$ encompass the mobility gap, inside which the chiral edge mode lives. As in Fig. 3 of the main text, the edge mode disappears when a pair of the two delocalized bulk states fall into the same energy.

For the generic situation described above, we can employ the same argument as in the main text, to derive an edge contribution to the thermal Hall conductivity,

$$\kappa_{xy} = -\frac{k_B^2 T}{h} \sum_j \left[C_2(g(\mathcal{E}_j^+, T)) - C_2(g(\mathcal{E}_j^-, T)) \right]. \quad (21)$$

Here the summation is taken over chiral edge modes; the integer j counts chiral edge modes at finite frequency. \mathcal{E}_j^+ and \mathcal{E}_j^- stand for a pair of two energies by which the j -th chiral edge mode is bounded (Fig. 9(b)). We define $\mathcal{E}_j^+ > \mathcal{E}_j^-$ when the j -th chiral edge mode is right-handed, while $\mathcal{E}_j^- > \mathcal{E}_j^+$ when the mode is left-handed. $C_2(x) \equiv \int_0^x dt \ln((1+t)/t)^2$ and $g(E, T)$ is the Bose distribution function.

The above expression is qualitatively consistent with the thermal magnon Hall conductivity in the clean limit, which was previously obtained based on the linear response theory¹⁴⁻¹⁸;

$$\kappa_{xy} = -\frac{k_B^2 T}{h} \sum_n \int \frac{d^2 \mathbf{k}}{(2\pi)^2} \Omega_n(\mathbf{k}) \left[C_2(g(\mathcal{E}_n(\mathbf{k}), T)) - \frac{\pi^2}{3} \right]. \quad (22)$$

Here $\mathcal{E}_n(\mathbf{k})$ and $\Omega_n(\mathbf{k})$ stand for the n -th magnon energy band and n -th band Berry's curvature, respectively. $\mathbf{k} \equiv (k_x, k_y)$ denotes the two-dimensional crystal momentum. The Chern integer is defined for each band as an integral of

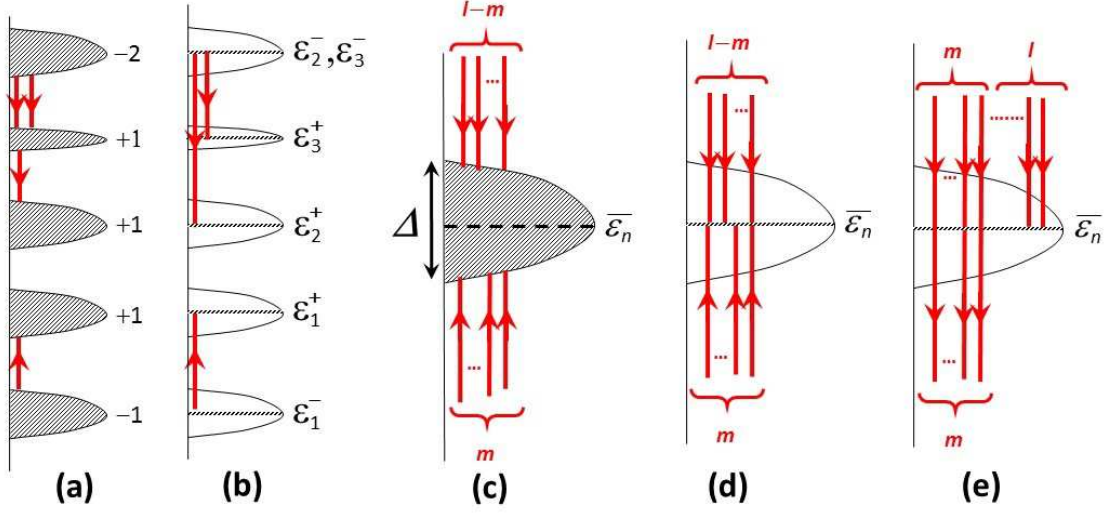


FIG. 9: Schematic picture for bulk magnon bands and chiral edge modes in the clean limit (a,c) and with disorders (b,d,e,f). The Chern integers for each magnon band are shown in (a) such as $-1, +1, +1, +1, -2$ (from below). A right/left-handed chiral edge mode is depicted by a red line with up/down-headed arrow respectively. Gray shadow regions denote extended bulk states, while the white region in the bands corresponds to mobility gaps. (c,d) the n -th band with $\text{Ch}(n) = l$, $\sum_{j=1}^{n-1} \text{Ch}(j) = -m$ and $l > m > 0$, (e) When the n -th band with $\text{Ch}(n) = l$, $\sum_{j=1}^{n-1} \text{Ch}(j) = m$ and $l > 0$, $m > 0$ is disordered.

the curvature in the first Brillouin zone (B.Z.);

$$\text{Ch}(n) \equiv \int_{\text{B.Z.}} \Omega_n(\mathbf{k}) \frac{d^2 \mathbf{k}}{2\pi}.$$

When all bulk magnon bands are fully gapped: $\mathcal{E}_n(\mathbf{k}) > 0$ for all \mathbf{k} and for all n , a sum of the Chern integers over band is zero⁵; $\sum_n \text{Ch}(n) = 0$. Thereby, Eq. (22) reduces to

$$\kappa_{xy} = -\frac{k_B^2 T}{h} \sum_n \int \frac{d^2 \mathbf{k}}{2\pi} \Omega_n(\mathbf{k}) C_2(g(\mathcal{E}_n(\mathbf{k}), T)). \quad (23)$$

Eq. (23) becomes identical to Eq. (21), when an energy band width of each bulk magnon band is much smaller than $k_B T$. In this limit, $\mathcal{E}_n(\mathbf{k})$ in the right hand side of Eq. (23) can be replaced by its band center energy $\bar{\mathcal{E}}_n$;

$$\lim_{\Delta \ll k_B T} \kappa_{xy} = -\frac{k_B^2 T}{h} \sum_n \int \frac{d^2 \mathbf{k}}{2\pi} \Omega_n(\mathbf{k}) C_2(g(\bar{\mathcal{E}}_n, T)) = -\frac{k_B^2 T}{h} \sum_n \text{Ch}(n) C_2(g(\bar{\mathcal{E}}_n, T)). \quad (24)$$

The equivalence between Eq. (21) and Eq. (24) can be seen with a help of the bulk-edge correspondence^{5,9,10}. For example, consider (i) the n -th bulk magnon band whose band center energy is $\bar{\mathcal{E}}_n$ and $\text{Ch}(n) = l$ and $\sum_{j=1}^{n-1} \text{Ch}(j) = -m$ with $l > m > 0$. The bulk-edge correspondence dictates that m pieces of right-handed chiral edge modes enter into the bulk band from below and $(l - m)$ pieces of left-handed chiral edge modes enter into the band from above (Fig. 9(c)). In the presence of small disorders, all the bulk states in the n -th band are localized except for the delocalized states at the band center $\bar{\mathcal{E}}_n$. Thereby, the delocalized bulk states at the band center terminate all the chiral edge modes; $\bar{\mathcal{E}}_n$ bounds the m pieces of right-handed chiral edge modes from above and the $(l - m)$ pieces of left-handed chiral edge modes from below (Fig. 9(d)). Let us consider another examples: (ii) the n -th band with $\text{Ch}(n) = l$, $\sum_{j=1}^{n-1} \text{Ch}(j) = m$ and $l > 0$, $m > 0$. In this case, the correspondence tells that m pieces of left-handed chiral edge modes pass by the band center energy $\bar{\mathcal{E}}_n$, while l pieces of left-handed chiral modes are terminated by the delocalized bulk states at $\bar{\mathcal{E}}_n$; $\bar{\mathcal{E}}_n$ bounds the latter l pieces of modes from below (Fig. 9(e)). By considering other cases as well and integrating them together, we can readily rewrite Eq. (24) into Eq. (21) in the small band width limit. Using $C_2(g(E = 0+)) = \frac{\pi^2}{3}$, we can further generalize the argument so far into a case with complete flat zero energy bands, $\mathcal{E}_n(\mathbf{k}) = 0$ for all \mathbf{k} and for $\exists n$, giving a consistency between Eq. (21) and Eq. (22) too.

The thermal Hall conductivity can be used to confirm the presence/absence of topological chiral edge modes in finite frequency regimes. For example, the thermal magnon Hall conductivity in the high temperature limit goes to a *non-zero* constant value ! Moreover, the value is given by a sum of those mobility gaps which bound topological chiral edge modes;

$$\lim_{T \rightarrow \infty} \kappa_{xy} = \frac{k_B}{h} \sum_j (\mathcal{E}_j^+ - \mathcal{E}_j^-). \quad (25)$$

Here the summation is over the edge modes; \mathcal{E}_j^+ and \mathcal{E}_j^- bound the j -th chiral edge mode in pair. Note that $\mathcal{E}_j^+ > \mathcal{E}_j^-$ for the right handed chiral edge mode and $\mathcal{E}_j^+ < \mathcal{E}_j^-$ for the left handed mode; right/left handed chiral mode contributes to positive/negative thermal Hall conductivity respectively. Nonetheless, there is no ‘topological’ reason which requires the sum in Eq. (25) to be zero. The non-zero κ_{xy} in the high temperature limit is quite unconventional. The feature clearly tells the presence of the chiral edge modes from otherwise in actual experimental systems.

-
- * Electronic address: rshindou@pku.edu.cn
- ¹ R. F. Wang, C. Nisoli, R. S. Freitas, J. Li, W. McConville, B. J. Cooley, M. S. Lund, N. Samarth, C. Leighton, V. H. Crespi and P. Schiffer, *Nature* **19**, 439 (2006).
 - ² J. H. P. Colpa, *Physica A* **93**, 327 (1978).
 - ³ D. J. Thouless, M. Kohmoto, M. P. Nightingale, and M. den Nijs, *Phys. Rev. Lett.* **49**, 405 (1982).
 - ⁴ M. Kohmoto, *Annals of Physics*, **160**, 343-354 (1985).
 - ⁵ R. Shindou, R. Matsumoto, S. Murakami and J. Ohe, *Phys. Rev. B*, **87**, 174427 (2013).
 - ⁶ G. Engelhardt, and T. Brandes, *Phys. Rev. A*, **91**, 053621, (2015).
 - ⁷ S. Furukawa, and M. Ueda, *New. J. Phys.* **17**, 115014 (2015).
 - ⁸ Z. F. Xu, L. You, A. Hemmerich, and W. V. Liu, arXiv:1602.04555v1.
 - ⁹ B. I. Halperin, *Phys. Rev. B*, **25**, 2185 (1982).
 - ¹⁰ Y. Hatsugai, *Phys. Rev. Lett.* **71**, 3697 (1993).
 - ¹¹ A. Serga, et. al. *Journal of Physics D: Applied Physics*, **43**, 264002 (2010).
 - ¹² M. Evers, C. A. Muller, and U. Nowak, *Phys. Rev. B* **92**, 014411 (2015).
 - ¹³ A. M. M. Pruisken, *The Quantum Hall Effect Second Edition*, ed. R. E. Prange, and S. M. Girvin (Springer-Verlag, New York, 1990), p. 112.
 - ¹⁴ R. Matsumoto and S. Murakami, *Phys. Rev. Lett.* **106**, 197202 (2011).
 - ¹⁵ R. Matsumoto and S. Murakami, *Phys. Rev. B*, **84**, 184406 (2011).
 - ¹⁶ R. Matsumoto, R. Shindou, and S. Murakami, *Phys. Rev. B*, **89**, 054420 (2014).
 - ¹⁷ T. Qin, Q. Niu and J. R. Shi, *Phys. Rev. Lett.* **107**, 236601 (2011).
 - ¹⁸ T. Qin, J. Zhou, and J. R. Shi, *Phys. Rev. B*, **86**, 104305 (2012).